Article

Superconductivity under pressure in a chromium-based kagome metal

https://doi.org/10.1038/s41586-024-07761-x

Received: 13 March 2024

Accepted: 26 June 2024

Published online: 28 August 2024

Check for updates

Yi Liu[1,2,13], Zi-Yi Liu[3,4,13], Jin-Ke Bao[5,6,13], Peng-Tao Yang[3,4], Liang-Wen Ji[1], Si-Qi Wu[1], Qin-Xin Shen[3,4], Jun Luo[3], Jie Yang[3], Ji-Yong Liu[7], Chen-Chao Xu[5], Wu-Zhang Yang[8], Wan-Li Chai[1], Jia-Yi Lu[1], Chang-Chao Liu[1], Bo-Sen Wang[3,4], Hao Jiang[9], Qian Tao[1], Zhi Ren[8], Xiao-Feng Xu[2], Chao Cao[1,10], Zhu-An Xu[1,11,12], Rui Zhou[3]✉, Jin-Guang Cheng[3,4]✉ & Guang-Han Cao[1,11,12]✉

Superconductivity in a highly correlated kagome system has been theoretically proposed for years (refs. 1–5), yet the experimental realization is hard to achieve[6,7]. The recently discovered vanadium-based kagome materials[8], which exhibit both superconductivity[9–11] and charge-density-wave orders[12–14], are nonmagnetic[8,9] and weakly correlated[15,16]. Thus these materials are unlikely to host the exotic superconductivity theoretically proposed. Here we report the discovery of a chromium-based kagome metal, $CsCr_3Sb_5$, which is contrastingly featured with strong electron correlations, frustrated magnetism and characteristic flat bands close to the Fermi level. Under ambient pressure, this kagome metal undergoes a concurrent structural and magnetic phase transition at 55 K, with a stripe-like $4a_0$ structural modulation. At high pressure, the phase transition evolves into two transitions, possibly associated with charge-density-wave and antiferromagnetic spin-density-wave orderings. These density-wave-like orders are gradually suppressed with pressure and, remarkably, a superconducting dome emerges at 3.65–8.0 GPa. The maximum of the superconducting transition temperature, $T_c^{max} = 6.4$ K, appears when the density-wave-like orders are completely suppressed at 4.2 GPa, and the normal state exhibits a non-Fermi-liquid behaviour, reminiscent of unconventional superconductivity and quantum criticality in iron-based superconductors[17,18]. Our work offers an unprecedented platform for investigating superconductivity in correlated kagome systems.

Materials with two-dimensional (2D) kagome lattice are featured with geometric frustration and characteristic electronic structures, from which various intriguing quantum states may emerge[19]. The vanadium-based kagome materials AV_3Sb_5 (A = K, Rb, Cs) recently discovered[8] present many exotic phenomena, including superconductivity[9–11,20], unusual charge order[12–14,21–24], anomalous Hall effect[25], pair density wave[26] and electronic nematicity[27]. Nevertheless, this class of materials are most likely phonon-mediated conventional superconductors[28], in line with the nonmagnetic nature and relatively weak electron correlations[8,9,15,16]. Correlated magnetic kagome materials, on the other hand, generally bear robust magnetism hampering the appearance of superconductivity. Below we report a new chromium-based kagome material, $CsCr_3Sb_5$, which uniquely hosts both strong electron correlations and fragile magnetism. We found that the density-wave-like orders are gradually suppressed with pressure, and superconductivity emerges near a quantum critical point (QCP) at $P_c \approx 4$ GPa.

Single crystals of $CsCr_3Sb_5$ were grown using a self-flux method[9,29]. The as-grown crystals were characterized by single-crystal X-ray diffractions (XRD) and energy dispersive X-ray (EDX) spectroscopy (Extended Data Fig. 1a). The crystals are typically thin flakes with silver metallic lustre and hexagonal morphology, and they are stable in air. The chemical composition is of stoichiometric $CsCr_3Sb_5$ within the measurement errors. The single-crystal XRD at room temperature (Extended Data Fig. 1b–d) shows that $CsCr_3Sb_5$ crystallizes in a hexagonal lattice with the space group of $P6/mmm$ (Fig. 1a and Extended Data Table 1). Cr atoms form a 2D kagome net with Sb1 atoms located at the centre of the hexagons. This 2D Cr_3Sb plane is sandwiched by the honeycomb-like layers of Sb2, and the resultant sandwiched layers of $[Cr_3Sb_5]^-$ are separated by layers of Cs^+ ions. Therefore, $CsCr_3Sb_5$ is isostructural to AV_3Sb_5 (ref. 8).

[1]School of Physics, Zhejiang University, Hangzhou, China. [2]Department of Applied Physics, Key Laboratory of Quantum Precision Measurement of Zhejiang Province, Zhejiang University of Technology, Hangzhou, China. [3]Beijing National Laboratory for Condensed Matter Physics and Institute of Physics, Chinese Academy of Sciences, Beijing, China. [4]School of Physical Sciences, University of Chinese Academy of Sciences, Beijing, China. [5]School of Physics and Hangzhou Key Laboratory of Quantum Matters, Hangzhou Normal University, Hangzhou, China. [6]Department of Physics, Materials Genome Institute and Shanghai Key Laboratory of High Temperature Superconductors, Shanghai University, Shanghai, China. [7]Department of Chemistry, Zhejiang University, Hangzhou, China. [8]School of Science, Westlake Institute for Advanced Study, Westlake University, Hangzhou, China. [9]School of Physics and Optoelectronics, Xiangtan University, Xiangtan, China. [10]Center for Correlated Matter, Zhejiang University, Hangzhou, China. [11]Interdisciplinary Center for Quantum Information, and State Key Laboratory of Silicon and Advanced Semiconductor Materials, Zhejiang University, Hangzhou, China. [12]Collaborative Innovation Centre of Advanced Microstructures, Nanjing University, Nanjing, China. [13]These authors contributed equally: Yi Liu, Zi-Yi Liu, Jin-Ke Bao. ✉e-mail: rzhou@iphy.ac.cn; jgcheng@iphy.ac.cn; ghcao@zju.edu.cn

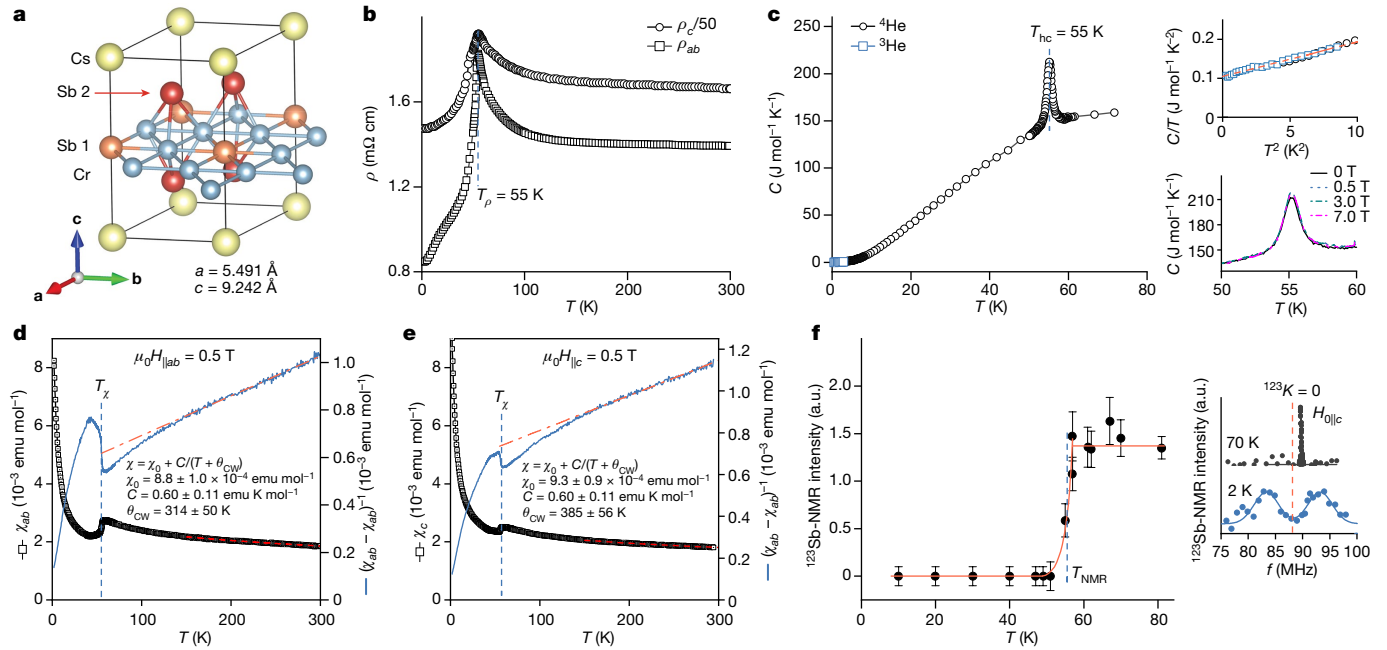

Fig. 1 | Crystal structure and physical properties of $CsCr_3Sb_5$. **a**, Unit cell of the high-temperature hexagonal phase of $CsCr_3Sb_5$. **b**, In-plane and out-of-plane resistivities as functions of temperature T. **c**, Temperature dependence of specific heat (C). The top right figure shows C/T versus T^2 at low temperatures, and the bottom right figure highlights the robustness of the $C(T)$ anomaly against magnetic fields along the c-axis. **d**,**e**, The temperature dependence of magnetic susceptibility χ with the magnetic field parallel (**d**) and perpendicular (**e**) to the ab plane. The right axis plots $(\chi-\chi_0)^{-1}$ versus T. The red dashed lines denote the Curie–Weiss fit, and the fitted parameters are shown. **f**, Temperature dependence of ^{123}Sb-NMR signal (corrected for a temperature factor $1/T$). The figure on the right is the ^{123}Sb-NMR spectra at 70 K and 2 K under an external field of $\mu_0H = 16$ T along the c-axis. The solid lines are the Gaussian fit. The red dashed line marks the average of the Knight shift at 2 K. In **b**–**f**, the anomalies at 55 K associated with the phase transition are marked with blue dashed lines. a.u., arbitrary units.

Figure 1b–f summarizes the physical properties of $CsCr_3Sb_5$ at ambient pressure. The in-plane resistivity $\rho_{ab}(T)$ is nearly temperature-independent above about 150 K with an absolute value of resistivity of 1.4 mΩ cm (Fig. 1b and Extended Data Fig. 1g). The resistivity anisotropy ρ_c/ρ_{ab} is as high as around 60, indicating a quasi-2D transport property. In the 2D-conduction scenario, the parameter k_Fl, where k_F and l are the Fermi wavevector and mean free path, respectively, is estimated to be close to unity[30], suggestive of a correlated bad metal[31]. The low-T specific-heat data (Fig. 1c, top right) give information about the strength of electron correlations. The data fitting with the formula $C/T = \gamma + \beta T^2$ yields a large electronic specific-heat coefficient, $\gamma_{exp} = 105(1)$ mJ K^{-1} mol^{-1}. This γ value is four times larger than that of the V-based CsV_3Sb_5 (ref. 32), and it is even larger than that of correlated quasi-one-dimensional superconductor $K_2Cr_3As_3$ (ref. 33).

Notably, a resistivity peak appears at $T_\rho = 55$ K. The corresponding anomaly is also manifested by a peak in the specific heat $C(T)$ (Fig. 1c), a drop in the magnetic susceptibility $\chi(T)$ (Fig. 1d,e) and changes in the magnetoresistance and Hall coefficient (Extended Data Fig. 1h–l). No obvious thermal hysteresis was observed at around 55 K. Putting all these observations together, we can conclude a second-order or weakly first-order phase transition for $CsCr_3Sb_5$.

The $\chi(T)$ data at high temperatures exhibit a Curie–Weiss (CW) behaviour (Fig. 1d,e), in contrast with the temperature-independent character in CsV_3Sb_5 (refs. 9,29). We thus fitted the data with the formula $\chi(T) = \chi_0 + C/(T + \theta_{CW})$, where C refers to Curie constant and θ_{CW} is paramagnetic CW temperature. The best fit yields an effective magnetic moment of $\mu_{eff} = 1.26 \pm 0.12\,\mu_B$ Cr^{-1}, where μ_B refers to the Bohr magneton, suggesting the existence of Cr local moment. The large positive value of θ_{CW} higher than 300 K (Fig. 1d,e) indicates strong AFM interactions between the Cr magnetic moments, which explains the robustness of the phase transition against external magnetic fields (Fig. 1c, bottom right). Note that the magnetic frustration index[34], $f = |\theta_{CW}|/T_N \approx 6$–$7$, is moderately large, suggesting notable magnetic frustrations that commonly exist in a magnetic kagome lattice.

The nuclear magnetic resonance (NMR) measurement gives evidence of an antiferromagnetic (AFM) ordering (Fig. 1f and Extended Data Fig. 2). The intensity of ^{123}Sb-NMR spectra decreases abruptly below $T_N \approx 55$ K, signalling a shift in spectral weight, which is a typical feature of magnetic transitions[35]. At 2 K, a marked change in NMR spectra was observed: from one narrow line to two broad peaks (Fig. 1f, right). This splitting of the NMR line strongly suggests an AFM order for the Cr spins because, in general, an AFM alignment of spins generates opposite internal magnetic fields at the Sb2 site. The severe spectral broadening dictates a large distribution of the internal magnetic field, implying that the magnetic structure should be somewhat complex. A recent theoretical study[36] suggests an altermagnetic order as the ground state for $CsCr_3Sb_5$. We also note that the Knight shift at 70 K is higher than that at 2 K (Fig. 1f, right), indicating that the spin susceptibility decreases with decreasing temperature. This result tells us that the observed magnetic susceptibility tail at low temperatures (Fig. 1d,e) is of extrinsic origin, possibly because of tiny paramagnetic impurities and/or lattice imperfections.

To understand the structural response of the phase transition in $CsCr_3Sb_5$, we performed the single-crystal XRD down to 40 K. As shown in Fig. 2a,b and Extended Data Fig. 3a–c, satellite reflections appear below about 55 K, apart from the primary Bragg diffractions in the **a***–**b*** plane. At first sight, these satellite spots seem to be related to a symmetry-equivalent triple-**Q** modulation vector that corresponds to a 4 × 4 superlattice based on the original hexagonal lattice. However, the intensities of the symmetry-related satellite spots by the six-fold rotation are significantly unequal. Therefore, the six-fold rotation symmetry of the hexagonal lattice is broken, and the diffraction pattern should be interpreted in terms of a multi-domain modulated structure with a single **Q** vector (1/4, 0, 0) based on a pseudo-hexagonal lattice.

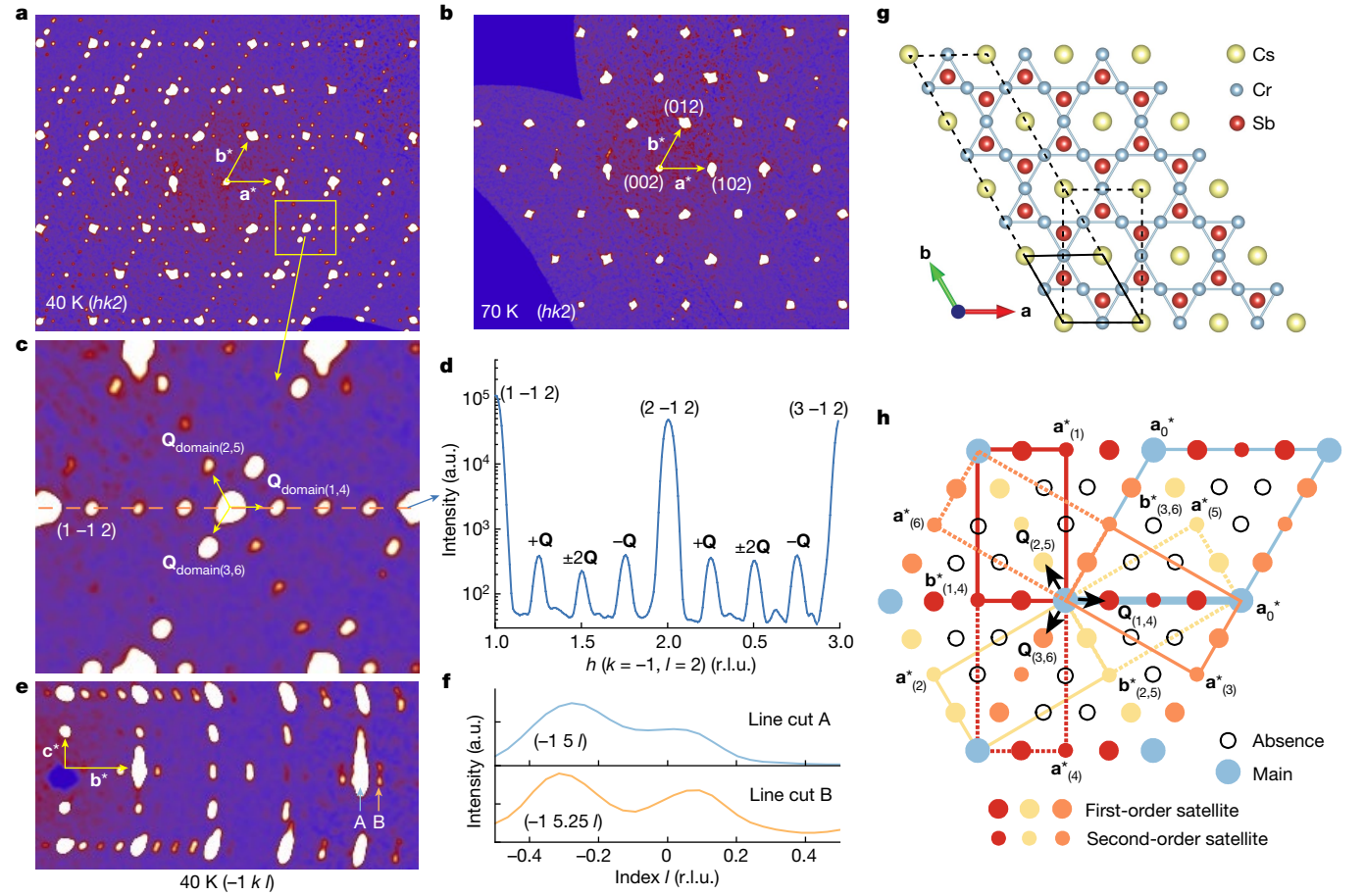

Fig. 2 | Structural modulations in $CsCr_3Sb_5$. **a**,**b**, Reconstructed (*hk*2) planes of reflections at 40 K (**a**) and 70 K (**b**), with unit vectors **a*** and **b*** marked. **c**, A close-up around the main reflection ($2\bar{1}2$) in **a**, highlighting the satellite reflections that are indexed by a single **Q**-vector with six twin domains. **d**, Cut along the blue dashed line marked in **c**. **e**, Reconstructed ($\bar{1}kl$) plane of reflections at 40 K. **f**, Line cuts along A and B marked in **e**. **g**, Crystal structure of $CsCr_3Sb_5$ viewed along the *c*-axis. The original hexagonal unit cell is marked by solid lines. The *C*-centred monoclinic and $a_0 \times 4a_0$ unit cells are marked with dashed lines. **h**, Schematics of the six monoclinic pseudo-orthohexagonal twin domains in the reciprocal lattice space projected along the [001] direction. $\mathbf{a}_0^*$ and $\mathbf{b}_0^*$ are the original unit cells. $\mathbf{a}_{(i)}^*$ and $\mathbf{b}_{(i)}^*$ ($i = 1$–6) represent the lattice units of six individual monoclinic twin domains. Domains 4–6 are marked with dashed lines for unit cells. $\mathbf{b}_{(1)}^*$, $\mathbf{b}_{(2)}^*$ and $\mathbf{b}_{(3)}^*$ share the same axis with $\mathbf{b}_{(4)}^*$, $\mathbf{b}_{(5)}^*$ and $\mathbf{b}_{(6)}^*$ in the projected view along **c***, respectively. Domains 1, 2 and 3 are connected by the three-fold rotation along **c***. Domains 1 and 4 (the same for other pairs of domains) are correlated by a two-fold rotation along **b*** because of the monoclinic distortion. The filled red, yellow and orange circles refer to satellite reflections attributed to $\mathbf{Q}_{(1,4)}$, $\mathbf{Q}_{(2,5)}$ and $\mathbf{Q}_{(3,6)}$, respectively. The satellite reflections of domains 1 and 4 are overlapped. The empty circles denote the absence of mixed-order satellite reflections between any two $\mathbf{Q}_i$ vectors in a hexagonal unit cell. a.u., arbitrary units. r.l.u., reciprocal lattice units.

This single-**Q** modulation is observed at 55 K before full recovery of the hexagonal phase at 70 K (Extended Data Fig. 3j–l). Furthermore, peak splittings are observed especially at high diffraction angles in the ($\bar{1}kl$) plane (Fig. 2e), as demonstrated by the line cuts along **c*** (Fig. 2f). This points to a two-fold rotation symmetry breaking along **b*** (Extended Data Fig. 3g,h). Notably, some mixed-order satellite spots between any two $\mathbf{Q}_i$ vectors are absent, indicating that these $\mathbf{Q}_i$ vectors are independent, coming from different domains. In the **b*****c*** plane, nevertheless, no additional satellite spots along **c*** direction are detected (Fig. 2e and Extended Data Fig. 3d–g), in conformity with the θ–2θ scan result shown in the Extended Data Fig. 1d–f. Combined with all the results above and following a group–subgroup law in space groups (Extended Data Fig. 3i), the low-temperature diffraction pattern can be equivalently interpreted by a modulated structure with a single **Q** vector of (0, 0.5, 0) based on the monoclinic lattice $a = a_0$, $b \approx \sqrt{3}a_0$, $c = c_0$ and $\alpha > 90°$.

As conduction electrons generally couple with the underlying lattice in a metallic system, the structural modulations suggest a charge-density-wave (CDW)-like instability[37] (Methods). Meanwhile, the magnetic susceptibility and NMR data above indicate an AFM ordering at the phase transition. Therefore, it is reasonable to conjecture a concurrent intertwined density-wave order for the ground state, in which charge, spin and lattice degrees of freedom couple together, something similar to the cases in the metal Cr (ref. 38) and the trilayer nickelate[39].

To explore possible superconductivity, we applied pressure to the crystals. Figure 3a shows the $\rho(T)$ data of $CsCr_3Sb_5$ under various pressures up to 12 GPa. We see that the resistivity decreases monotonically with pressure, and the metallicity is steadily enhanced. At $P > 1$ GPa, the resistivity peak evolves into two anomalies at T_1 and T_2, respectively (Extended Data Fig. 4). There is a remarkable resistivity jump at T_1, implying a CDW ordering because the latter generally opens an energy gap. Comparatively, the anomaly at T_2 is rather mild, which can be attributed to a spin-density-wave (SDW) ordering. If so, the structural modulation and/or distortion expected at T_1 will release the geometric frustration, which helps the AFM ordering at T_2. With increasing pressure, both T_1 and T_2 decrease monotonically, and superconductivity gradually emerges at $P > 3.60$ GPa. At 3.65 GPa and 3.80 GPa, both superconducting and density-wave-like transitions are observed (Extended Data Figs. 4l,m and 5d), suggesting the coexistence of superconductivity and magnetism. At 4 GPa ≤ P ≤ 8 GPa,

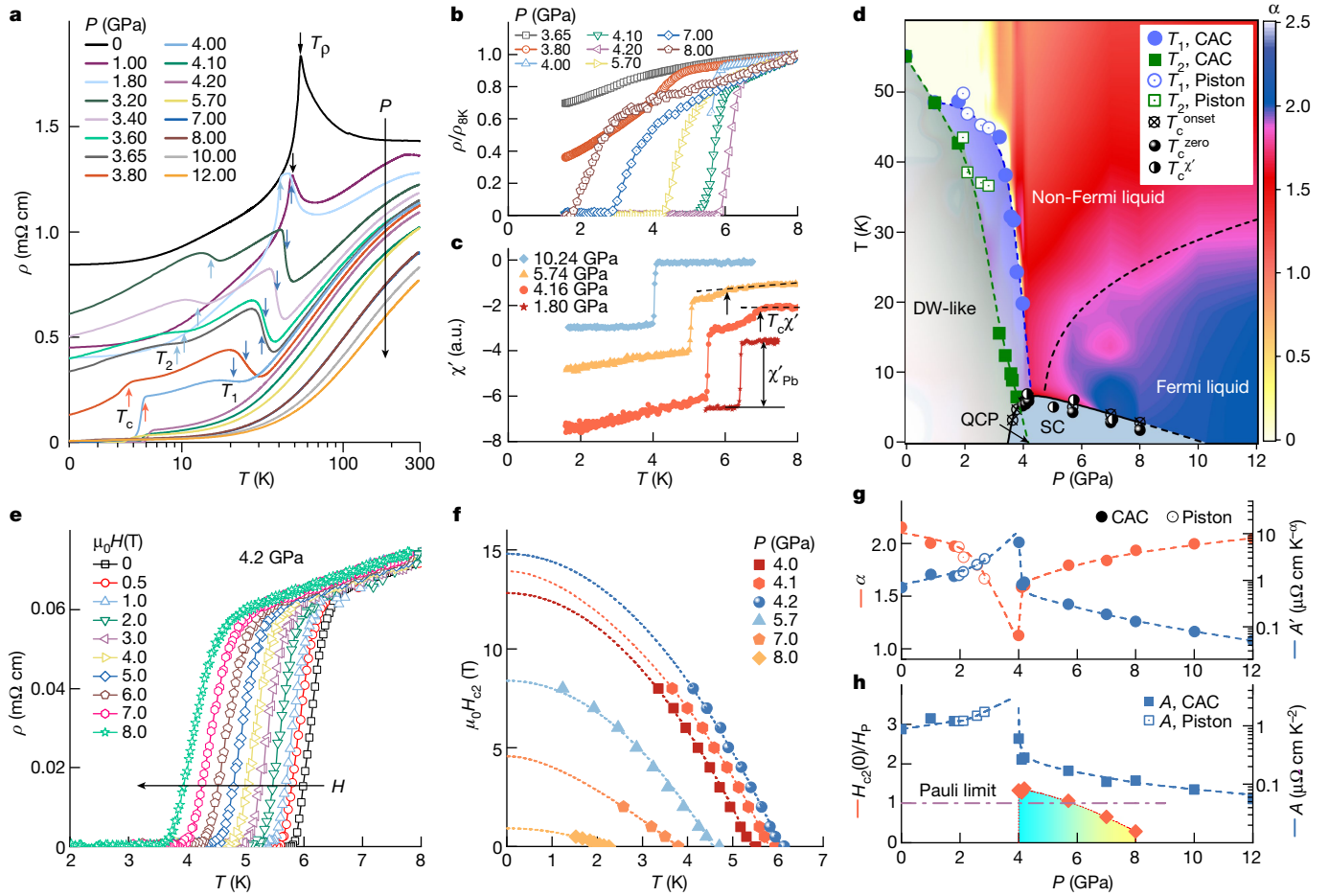

Fig. 3 | Superconductivity emerging from density-wave-like orders in $CsCr_3Sb_5$. **a**, $\rho(T)$ curves under high pressures. The blue, olive and red arrows mark CDW-like, SDW-like and superconducting transitions at T_1, T_2 and T_c, respectively. **b**, Superconducting transitions at different pressures. **c**, Temperature dependence of a.c. susceptibility, χ', under high pressures. A piece of superconducting Pb was placed together with the sample as a reference material. **d**, The electronic P–T phase diagram. DW, density wave; QCP, quantum critical point; and SC, superconductivity. **e**, Superconducting transitions under various magnetic fields at 4.2 GPa. **f**, Upper critical fields as functions of temperature. **g**, Power α (left axis) and the coefficient A' (right axis) as functions of pressure (see the text for details). **h**, The relative upper critical field to the Pauli-limited field (left axis) and the coefficient A of the T-square term in $\rho = \rho_0 + AT^2$ (right axis) as functions of pressure.

the superconducting transitions are more clearly seen in Fig. 3b with zero resistance, and bulk superconductivity is confirmed by the a.c. magnetic susceptibility (χ') measurement (Fig. 3c and Extended Data Fig. 5a–c) with the highest superconducting transition temperature of 6.4 K at 4.2 GPa. For $P \geq 10$ GPa, no superconductivity can be observed down to 1.6 K.

Figure 3e shows the superconducting transitions under different magnetic fields at 4.2 GPa (more data are shown in Extended Data Fig. 5d–i). As expected, T_c shifts to lower temperatures with increasing fields. Here we used the criteria of 50% of normal-state resistivity for determining $T_c(H)$, from which the upper critical fields $\mu_0H_{c2}(T)$ are derived (Fig. 3f). The $\mu_0H_{c2}(T)$ data can be well described by the equation, $H_{c2}(T) = H_{c2}(0)[1 - (T/T_c)^2]$. The fitted zero-temperature $\mu_0H_{c2}(0)$ values are 11.95 T and 14.34 T for $P = 4.0$ and 4.2 GPa, respectively, which exceed the Pauli limit of $\mu_0H_P \approx 1.84T_c$ (in tesla). Note that field direction was not sure for the present measurement, thus the anisotropy of $H_{c2}(T)$ is left for future study.

With the above results, the electronic P–T phase diagram for $CsCr_3Sb_5$ is established (Fig. 3d). At ambient pressure, there is a CDW-like and SDW-like ordering at 55 K. When the applied pressure exceeds about 1 GPa, it evolves into two successive transitions, probably associated with CDW and SDW orderings, respectively. Both the density-wave-like transition temperatures, T_1 and T_2, are suppressed gradually before going to absolute zero. The critical pressure at $T_2 \to 0$ is extrapolated to be $P_c \approx 4.2$ GPa, at which T_c and $H_{c2}(0)$ achieve their maximal values. Moreover, there is a narrow region of 3.6 GPa $< P <$ 4.1 GPa, in which superconductivity probably coexists with the density-wave-like orders. All these results resemble those of iron-based superconductors[17,18], CrAs (ref. 40) and MnP (ref. 41), pointing to quantum criticality in the present system.

One of the most important hallmarks of quantum criticality is a non-Fermi-liquid (or, strange-metal) behaviour, which is observed from the normal-state resistivity just above T_c. The data fitting (Extended Data Fig. 6a) with the power law $\rho = \rho_0' + A'T^\alpha$ shows that, at 4 GPa, α reaches about 1.0, distinct from about 2.0 at the lower and higher pressures (Fig. 3g), suggesting the breakdown of Fermi-liquid state at around the QCP (ref. 42). The detailed variations of α are also shown in the coloured contour plot, in which the non-Fermi-liquid regime is marked. If assuming Fermi-liquid scenario in the low-temperature limit, alternatively, the data fitting with the formula $\rho = \rho_0 + AT^2$ (Extended Data Fig. 6b) yields a remarkable enhancement of the coefficient A (Fig. 3h) at $P \to 4$ GPa. A similar divergence behaviour is seen for the parameter A' (Fig. 3g). This result further corroborates a QCP at around 4 GPa. Furthermore, the large value of A actually suggests unconventional superconductivity in pressurized $CsCr_3Sb_5$, because the T_c/T_F (T_F is the Fermi temperature) values estimated just lie in the unconventional

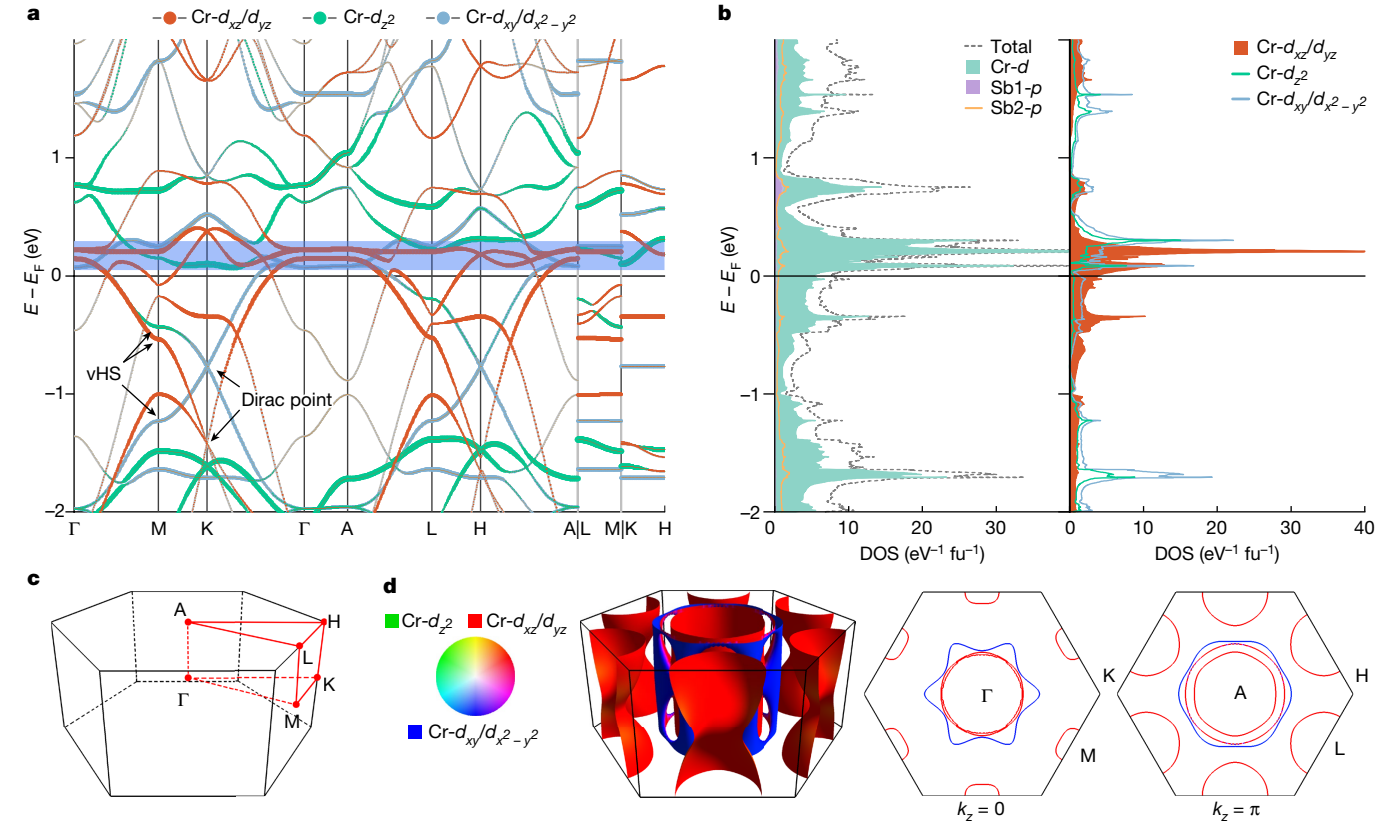

Fig. 4 | Electronic structure of $CsCr_3Sb_5$ by DFT calculations. a, The band structure highlighting contributions from Cr-d_{xz}/d_{xz}, Cr-$d_{xy}/d_{x^2-y^2}$ and Cr-d_{z^2} orbitals. The van Hove singularity (vHS) and the Dirac point are indicated by the arrows, and the flat bands are marked by the transparent blue band. **b**, Density of states (DOS) contributed from each atom (left) and different Cr-3*d* orbitals (right). **c**, The Brillouin zone with high-symmetry points marked. **d**, The merged Fermi-surface sheets (left), Fermi-surface slices at $k_z = 0$ (middle) and π (right). The red, blue and green colours denote the Cr-d_{xz}/d_{xz}, Cr-$d_{xy}/d_{x^2-y^2}$ and Cr-d_{z^2} components, respectively.

superconductor region covering cuprates, iron-based pnictides and chalcogenides, and heavy-fermion materials (Extended Data Fig. 7).

Next, we show the first-principles density-functional-theory (DFT) calculation results for the high-temperature hexagonal phase of $CsCr_3Sb_5$. The calculated band structure (Fig. 4a), which highlights the components of distinct Cr-3*d* orbitals, shows a metallic behaviour with three bands crossing the Fermi level, E_F. As a result, two hole-type Fermi surfaces around the ΓA line and one electron-type Fermi surface around the ML line are derived (Fig. 4c,d). All the Fermi-surface sheets are quasi-2D, which explains the large anisotropy of resistivity. For d_{xz}/d_{yz} and $d_{xy}/d_{x^2-y^2}$ derived bands, notably, they show characteristic kagome-like electronic structures with van Hove singularities, Dirac points and flat bands. These flat bands, which are marked with the blue stripe, are distorted along certain directions owing to the anisotropic hoppings between different 3*d* orbitals and the hybridization between Cr-kagome and Sb2-honeycomb lattices.

In contrast to the case of CsV_3Sb_5 (Extended Data Fig. 8c), the Fermi level in $CsCr_3Sb_5$ is only about 0.1 eV lower below the nearest flat band and about 0.5 eV higher above the van Hove points. Meanwhile, the Fermi-surface topology is very distinct from that of CsV_3Sb_5 (refs. 9,13). Under a pressure of 5 GPa, the flat bands move up with valence bandwidths moderately broadened (Extended Data Fig. 8d). As a consequence, the system undergoes a Lifshitz transition[43], in which the quasi-2D Fermi surface around the ML line breaks into a large electron pocket (around the L point) and a tiny hole pocket (around the M point). This variation in electronic structure might be in relation to the suppression of density-wave-like orders with applied pressure.

The electronic states at around E_F are mostly contributed from the Cr-3*d* orbitals (Fig. 4b). Among them, Cr-3d_{xz}/d_{xz} and Cr-3$d_{xy}/d_{x^2-y^2}$ dominate the states at E_F. The total density of states at E_F is $D(E_F) = 7.7$ states eV^{-1} fu^{-1}. This $D(E_F)$ value corresponds to an electronic specific-heat coefficient of $\gamma_0 = (1/3)\pi k_B^2 D(E_F) = 18.1$ mJ K^{-2} mol^{-1}, which is only about one-sixth of the experimental result. Note that the bare $D(E_F)$ should be somewhat lower because of the density-wave-like order. This means that the correlation-induced electron-mass renormalization factor could be even larger.

We demonstrated that $CsCr_3Sb_5$ exhibits contrastingly different properties in comparison with its structurally analogous compound CsV_3Sb_5 (Extended Data Table 2). This can be summarized as follows: (1) $CsCr_3Sb_5$ behaves as a correlated metal with a large electron-mass renormalization and substantial magnetic frustration. It undergoes a phase transition at 55 K associated with AFM density-wave-like ordering at ambient pressure. (2) The density-wave-like order has a single-**Q** modulation with a 4 × 1 × 1 supercell based on a pseudo-hexagonal lattice. (3) Under high pressure, a superconducting dome emerges near a QCP at about 4.2 GPa. This is in contrast with the AV_3Sb_5 family, which exhibits superconductivity already at ambient pressure and, with applying pressure, superconductivity does not disappear[44–46].

As is known, unconventional superconductivity typically emerges from a spin- and/or charge-ordered state in a correlated electron system, as exemplified in cuprates, iron-based pnictides and chalcogenides, and heavy-fermion materials[47–49]. Here $CsCr_3Sb_5$ shows similarities with the known unconventional superconductors in terms of electron correlations, evolution of superconductivity, intertwined orders and the T_c/T_F value in particular. This possible realization of unconventional superconductivity in the chromium-based correlated kagome metal is a unique example, which may shed light on the mechanism of unconventional superconductivity from a distinct perspective.

Online content

Any methods, additional references, Nature Portfolio reporting summaries, source data, extended data, supplementary information, acknowledgements, peer review information; details of author contributions and competing interests; and statements of data and code availability are available at https://doi.org/10.1038/s41586-024-07761-x.

1. Ko, W.-H., Lee, P. A. & Wen, X.-G. Doped kagome system as exotic superconductor. *Phys. Rev. B* **79**, 214502 (2009).
2. Yu, S.-L. & Li, J.-X. Chiral superconducting phase and chiral spin-density-wave phase in a Hubbard model on the kagome lattice. *Phys. Rev. B* **85**, 144402 (2012).
3. Wang, W.-S., Li, Z.-Z., Xiang, Y.-Y. & Wang, Q.-H. Competing electronic orders on kagome lattices at van Hove filling. *Phys. Rev. B* **87**, 115135 (2013).
4. Kiesel, M. L., Platt, C. & Thomale, R. Unconventional Fermi surface instabilities in the kagome Hubbard model. *Phys. Rev. Lett.* **110**, 126405 (2013).
5. Zhou, Y., Kanoda, K. & Ng, T.-K. Quantum spin liquid states. *Rev. Mod. Phys.* **89**, 025003 (2017).
6. Norman, M. R. *Colloquium*: herbertsmithite and the search for the quantum spin liquid. *Rev. Mod. Phys.* **88**, 041002 (2016).
7. Kelly, Z. A., Gallagher, M. J. & McQueen, T. M. Electron doping a kagome spin liquid. *Phys. Rev. X* **6**, 041007 (2016).
8. Ortiz, B. R. et al. New kagome prototype materials: discovery of KV_3Sb_5, RbV_3Sb_5, and CsV_3Sb_5. *Phys. Rev. Mater.* **3**, 094407 (2019).
9. Ortiz, B. R. et al. Cs V_3Sb_5: a $\mathbb{Z}_2$ topological kagome metal with a superconducting ground state. *Phys. Rev. Lett.* **125**, 247002 (2020).
10. Ortiz, B. R. et al. Superconductivity in the $\mathbb{Z}_2$ kagome metal KV_3Sb_5. *Phys. Rev. Mater.* **5**, 034801 (2021).
11. Yin, Q. et al. Superconductivity and normal-state properties of kagome metal RbV3Sb5 single crystals. *Chin. Phys. Lett.* **38**, 037403 (2021).
12. Jiang, Y.-X. et al. Unconventional chiral charge order in kagome superconductor KV_3Sb_5. *Nat. Mater.* **20**, 1353–1357 (2021).
13. Ortiz, B. R. et al. Fermi surface mapping and the nature of charge-density-wave order in the kagome superconductor CsV_3Sb_5. *Phys. Rev. X* **11**, 041030 (2021).
14. Liang, Z. et al. Three-dimensional charge density wave and surface-dependent vortex-core states in a kagome superconductor CsV_3Sb_5. *Phys. Rev. X* **11**, 031026 (2021).
15. Zhao, J., Wu, W., Wang, Y. & Yang, S. A. Electronic correlations in the normal state of the kagome superconductor KV_3Sb_5. *Phys. Rev. B* **103**, L241117 (2021).
16. Luo, H. et al. Electronic nature of charge density wave and electron-phonon coupling in kagome superconductor KV_3Sb_5. *Nat. Commun.* **13**, 273 (2022).
17. Colombier, E., Bud'ko, S. L., Ni, N. & Canfield, P. C. Complete pressure-dependent phase diagrams for $SrFe_2As_2$ and $SrFe_2As_2$. *Phys. Rev. B* **79**, 224518 (2009).
18. Shibauchi, T., Carrington, A. & Matsuda, Y. A quantum critical point lying beneath the superconducting dome in iron pnictides. *Annu. Rev. Condens. Matter Phys.* **5**, 113–135 (2014).
19. Yin, J.-X., Lian, B. & Hasan, M. Z. Topological kagome magnets and superconductors. *Nature* **612**, 647–657 (2022).
20. Zhong, Y. et al. Nodeless electron pairing in CsV_3Sb_5-derived kagome superconductors. *Nature* **617**, 488–492 (2023).
21. Neupert, T., Denner, M. M., Yin, J.-X., Thomale, R. & Hasan, M. Z. Charge order and superconductivity in kagome materials. *Nat. Phys.* **18**, 137–143 (2022).
22. Kang, M. et al. Twofold van Hove singularity and origin of charge order in topological kagome superconductor CsV_3Sb_5. *Nat. Phys.* **18**, 301–308 (2022).
23. Zhao, H. et al. Cascade of correlated electron states in the kagome superconductor CsV_3Sb_5. *Nature* **599**, 216–221 (2021).
24. Mielke, C.III et al. Time-reversal symmetry-breaking charge order in a kagome superconductor. *Nature* **602**, 245–250 (2022).
25. Yang, S.-Y. et al. Giant, unconventional anomalous Hall effect in the metallic frustrated magnet candidate, KV_3Sb_5. *Sci. Adv.* **6**, eabb6003 (2020).
26. Chen, H. et al. Roton pair density wave in a strong-coupling kagome superconductor. *Nature* **599**, 222–228 (2021).
27. Nie, L. et al. Charge-density-wave-driven electronic nematicity in a kagome superconductor. *Nature* **604**, 59–64 (2022).
28. Jiang, K. et al. Kagome superconductors AV_3Sb_5 (A=K, Rb, Cs). *Natl Sci. Rev.* **10**, nwac199 (2022).
29. Liu, Y. et al. Enhancement of superconductivity and suppression of charge-density wave in As-doped CsV_3Sb_5. *Phys. Rev. Mater.* **6**, 124803 (2022).
30. Johnston, D. C. The puzzle of high temperature superconductivity in layered iron pnictides and chalcogenides. *Adv. Phys.* **59**, 803–1061 (2010).
31. Emery, V. J. & Kivelson, S. A. Superconductivity in bad metals. *Phys. Rev. Lett.* **74**, 3253–3256 (1995).
32. Duan, W. et al. Nodeless superconductivity in the kagome metal CsV_3Sb_5. *Sci. China Phys. Mech. Astron.* **64**, 107462 (2021).
33. Bao, J.-K. et al. Superconductivity in quasi-one-dimensional $K_2Cr_3As_3$ with significant electron correlations. *Phys. Rev. X* **5**, 011013 (2015).
34. Ramirez, A. Strongly geometrically frustrated magnets. *Annu. Rev. Mater. Sci.* **24**, 453–480 (1994).
35. Kitagawa, K., Katayama, N., Ohgushi, K., Yoshida, M. & Takigawa, M. Commensurate itinerant antiferromagnetism in $BaFe_2As_2$: ^{75}As-NMR studies on a self-flux grown single crystal. *J. Phys. Soc. Jpn.* **77**, 114709 (2008).
36. Xu, C. et al. Frustrated altermagnetism and charge density wave in kagome superconductor $CsCr_3Sb_5$. Preprint at arxiv.org/abs/2309.14812 (2023).
37. Zhu, X., Zhang, J., Guo, J. & Plummer, E. W. Misconceptions associated with the origin of charge density waves. *Adv. Phys. X* **2**, 622–640 (2017).
38. Hu, Y. et al. Real-space observation of incommensurate spin density wave and coexisting charge density wave on Cr (001) surface. *Nat. Commun.* **13**, 445 (2022).
39. Zhang, J. et al. Intertwined density waves in a metallic nickelate. *Nat. Commun.* **11**, 6003 (2020).
40. Wu, W. et al. Superconductivity in the vicinity of antiferromagnetic order in CrAs. *Nat. Commun.* **5**, 5508 (2014).
41. Cheng, J.-G. et al. Pressure induced superconductivity on the border of magnetic order in MnP. *Phys. Rev. Lett.* **114**, 117001 (2015).
42. Löhneysen, H. V., Rosch, A., Vojta, M. & Wölfle, P. Fermi-liquid instabilities at magnetic quantum phase transitions. *Rev. Mod. Phys.* **79**, 1015–1075 (2007).
43. Lifshitz, I. M. Anomalies of electron characteristics of a metal in the high pressure region. *Sov. Phys. J. Exp. Theor. Phys.* **11**, 1130–1135 (1960).
44. Zheng, L. et al. Emergent charge order in pressurized kagome superconductor CsV_3Sb_5. *Nature* **611**, 682–687 (2022).
45. Zhang, Z. et al. Pressure-induced reemergence of superconductivity in the topological kagome metal CsV_3Sb_5. *Phys. Rev. B* **103**, 224513 (2021).
46. Chen, K. Y. et al. Double superconducting dome and triple enhancement of T_c in the kagome superconductor CsV_3Sb_5 under high pressure. *Phys. Rev. Lett.* **126**, 247001 (2021).
47. Scalapino, D. J. A common thread: the pairing interaction for unconventional superconductors. *Rev. Mod. Phys.* **84**, 1383–1417 (2012).
48. Stewart, G. R. Unconventional superconductivity. *Adv. Phys.* **66**, 75–196 (2017).
49. Norman, M. R. The challenge of unconventional superconductivity. *Science* **332**, 196–200 (2011).

Methods

Crystal growth and characterizations

Single crystals of $CsCr_3Sb_5$ were grown using a self-flux method from the constituent elements Cs (Alfa 99.999%), Cr (Alfa 99.99%) and Sb (Aladdin 99.999%). Eutectic composition in the $CsSb–CsSb_2$ quasi-binary system was used as the flux. Mixtures of Cs, Cr and Sb in molar ratios of 9:2:18 were loaded into an alumina crucible, and it was sealed in a Ta tube by arc welding under an argon atmosphere. The Ta tube was protected from oxidation by sealing in an evacuated silica ampoule. The sample loaded assembly was slowly heated in a furnace to 900 °C holding for 18 h, and subsequently cooled slowly at a rate of 2 °C h^{-1} to 600 °C. Thin crystalline flakes in hexagonal shape could be easily harvested after the melts were immersed in water-free ethanol at room temperature for 48 h. The harvested crystals were stable in air with sizes up to 0.50 × 0.50 × 0.02 mm^3.

Single-crystal XRD was carried on a Bruker D8 Venture diffractometer with Mo Kα radiation. A piece of $CsCr_3Sb_5$ crystal with dimensions of 0.018 × 0.168 × 0.172 mm^3 was mounted on the sample holder using the oil of polybutenes. A flow of cryogenic helium gas was used to cool the crystal from room temperature to 40 K first and then to warm up to 50 K and 70 K successively. We also measured another piece of the crystal at 55 K, 58 K and 70 K. A full dataset was collected at each temperature. The data reduction, including integration and scaling, was done using the commercial software package APEX4. The reconstructed images in the reciprocal space from the raw frames were produced using the reciprocal unit vectors of the hexagonal lattice by the software CrysAlis^{Pro} (CrysAlis Pro v.171.40.53, Rigaku Oxford Diffraction). The crystal structure of $CsCr_3Sb_5$ was initially solved by SUPERFLIP (ref. 50) and then refined against the structure factor F in JANA2006 (ref. 51). We also performed θ–2θ scan on a PANalytical X-ray diffractometer (Model EMPYREAN) with a monochromatic $CuK\alpha_1$ radiation, which generates the (00l) diffraction pattern. The chemical composition of the as-grown crystals was determined using EDX spectroscopy on a scanning electron microscope (Hitachi S-3700N) equipped with Oxford Instruments X-Max spectrometer.

The low-temperature XRD on $CsCr_3Sb_5$ indicates a structural modulation below 55 K, which suggests CDW-like ordering. Here we use the phenomenological definition of CDW[37]. Namely, a CDW refers to modulation of the electron density regardless of its origin. The phrase 'CDW-like' is used to indicate that the origin of the structural modulation is not clear currently. In conventional quasi-one-dimensional CDW materials, structural modulation is caused by the electronic instability associated with Fermi-surface nesting. However, the chromium-based kagome metal studied here is quasi-2D with notable electron correlations. Thus, the origin of the structural modulation seems to be more complicated, and the electron correlations may play an important part in the CDW-like order[37].

Physical property measurements

The measurements of electrical resistivity, magneto-resistivity, Hall effect and specific heat were carried out on a physical property measurement system (PPMS-9, Quantum Design). The resistivity was measured by a standard four-terminal method using silver paste for making the electrodes. For the measurement of $\rho_c(T)$, the electrodes were made on both sides of the crystal, and the current electrodes were prominently larger than the voltage ones, such that the electric current flows homogeneously along the c-axis. The Hall coefficient and magnetoresistance with the magnetic field parallel to the c-axis were simultaneously measured on a nearly square-shaped crystal with a six-electrode configuration. The resistance and Hall signals were obtained, respectively, by symmetrizing and antisymmetrizing the data collected in reversed magnetic fields. Specific heat was measured using the thermal relaxation method with dozens of crystals (total mass was 0.29 mg). The samples were glued on the heat capacity puck with N grease. The data of addenda were measured in advance. The measurements were carried out for three times at each temperature, and the final $C(T)$ data were obtained by averaging. The temperature-rise parameter was set to the minimal value of 1% in the PPMS-9 for the best temperature resolution.

The magnetic measurements were performed on a magnetic property measurement system (MPMS-3, Quantum Design). Samples with a mass of 0.17 mg were carefully mounted on the sample holder. For the measurements with field perpendicular to the c-axis, pieces of crystals were attached to the quartz paddle with a little N grease. For the measurements with the field parallel to the c-axis, an additional high-purity quartz plate was used to hold the samples. The quartz plate was stuck to the quartz paddle with GE varnish. The assembly without samples was measured in advance as addenda. The $\chi(T)$ data in the range of 150 K < T < 300 K were fitted with the formula $\chi(T) = \chi_0 + C/(T + \theta_{CW})$ (see the main text). To avoid unreliable results due to the mutual dependence among the three parameters, we carried out the data fitting with the constraint assuming the same C value for the two field directions.

The NMR measurements were performed with a phase-coherent pulsed NMR spectrometer. To get sufficient NMR signal intensity, the $^{121/}$Sb- and ^{123}Sb-NMR spectra were measured on a collection of about 20 single crystals (around 0.1 mg) acquired by sweeping the frequency point by point and integrating the spin-echo signal. We stacked the single-crystal flakes along the c-direction, ensuring the applied magnetic field along the c-axis. Above $\mu_0 H = 16$ T, the NMR measurements were conducted by using the 26-T high-field NMR system at SECUF.

There are two types of Sb sites in $CsCr_3Sb_5$. Sb1 is located at the centre of the chromium hexagon, whereas Sb2 is located above the chromium triangle (Extended Data Fig. 2a). In principle, we should observe two NMR central lines. However, owing to the small quantity of the sample used for NMR experiments, we had a poor signal-to-noise ratio, and only one line is visible in ^{121}Sb- and ^{123}Sb-NMR spectra (Extended Data Fig. 2c). Given that the atomic ratio between Sb1 and Sb2 is 1:4, it is most likely that the observed line is from the Sb2 site.

^{123}Sb nuclei ($I = 7/2$) have a quadrupole moment Q that couples to the electric field gradient. This interaction is responsible for the second-order quadrupolar shift of the central line that adds to the Knight shift K. The total frequency shift can be expressed as, $\frac{f-f_0}{f_0} = K + \frac{\upsilon_c^2 \eta^2}{12(1+K)f_0^2}$, where $f_0 = {}^{123}\gamma H_0$ is the reference frequency, and $^{123}\gamma$ is the gyromagnetic ratio of ^{123}Sb. υ_c is the component of the quadrupole coupling tensor along its main axis (z along the crystallographic c-direction) and $\eta = \left| \frac{V_{XX} - V_{YY}}{V_{ZZ}} \right|$ is the asymmetry parameter of the EFG tensor V. As Sb2 site in $CsCr_3Sb_5$ has a similar environment as in CsV_3Sb_5, the asymmetry parameter η should also be zero at high temperatures[52]. By measuring the NMR frequency at different fields, the value of η is found to be zero from the slopes of $(f - f_0)/f_0$ versus f_0^{-2} (Extended Data Fig. 2b). All of these observations indicate that the NMR line being observed originates from the Sb2 site.

The high-pressure experiments were carried out at the CAC station of SECUF. A standard four-probe method was used for resistivity measurements under high pressure in CAC. The sample was hung inside a Teflon capsule filled with glycerol pressure-transmitting medium (PTM). The three-axis compression geometry together with the adoption of liquid PTM can ensure excellent pressure homogeneity. The pressure values in CAC were estimated from the pressure-loading force calibration curve predetermined at room temperature. The mutual induction method was used for the a.c. magnetic susceptibility measurements in CAC. Several pieces of thin samples together with a piece of Pb served as the pressure marker, and the superconducting reference were put inside the handmade primary and secondary coils of about 50 turns for each. The primary coil is driven by an a.c. current of 1 mA and 317.7 Hz, whereas the output signal from the secondary coil was measured with a lock-in amplifier Stanford SR 830. Details about the sample assembly and pressure calibrations of CAC can be found

elsewhere[53]. We also used a piston-type high-pressure cell to fine-tune the pressures in the range of 2 GPa < P < 3 GPa. Daphne 7373 was used as the PTM and the pressure values were determined from the superconducting transition temperature of Pb according to the formula $P = (7.20 - T_c^{Pb})/0.365$ GPa.

Electronic structure calculations

The DFT-based first-principles calculations were performed using the Vienna ab initio simulation package[54]. The Kohn–Sham wave functions were treated with the projected augmented wave method[55]. The exchange-correlation energy was calculated with a Perdew–Burke–Ernzerhof-type functional[56]. The energy cutoff of the plane-wave basis was up to 500 eV and a Γ-centred 12 × 12 × 8 k-point mesh was used in the self-consistent calculations. The experimental room-temperature crystal structure was adopted for the ambient-pressure calculations. As for the high-pressure calculations, the lattice constants and atomic coordinates were fully relaxed with a solid revised PBE (PBEsol) functional[57], leading to the calculated structural parameters of a = 5.272 Å, c = 8.400 Å and z(Sb2) = 0.2428. The Fermi surface (plotted with FermiSurfer program[58]) and orbital occupation results are calculated from our 30-band tight-binding Hamiltonians, which are obtained by Wannier downfolding[59]. As shown in Extended Data Fig. 8a, the band structures around the Fermi level are well reproduced with the Wannier downfolding results. During the Wannier downfolding processes, band disentanglements are performed with initial projectors of 15 Cr(V)-3d and 15 Sb-5p orbitals. The local coordinates are chosen so that the relative directions of Cr(V)-3d orbitals are identical with respect to the three-fold rotation axis (Extended Data Fig. 8b).

Data availability

The data shown in the main figures are provided in the Source data. Source data are provided with this paper.

50. Palatinus, L. & Chapuis, G. *SUPERFLIP* - a computer program for the solution of crystal structures by charge flipping in arbitrary dimensions. *J. Appl. Crystallogr.* **40**, 786–790 (2007).
51. Petricek, V., Dusek, M. & Palatinus, L. Crystallographic computing system JANA2006: general features. *Z. Kristallogr. Cryst. Mater.* **229**, 345–352 (2014).
52. Luo, J. et al. Possible star-of-David pattern charge density wave with additional modulation in the kagome superconductor CsV_3Sb_5. *npj Quantum Mater.* **7**, 30 (2022).
53. Cheng, J. G. et al. Integrated-fin gasket for palm cubic-anvil high pressure apparatus. *Rev. Sci. Instrum.* **85**, 093907 (2014).
54. Kresse, G. & Furthmüller, J. Efficient iterative schemes for *ab initio* total-energy calculations using a plane-wave basis set. *Phys. Rev. B* **54**, 11169–11186 (1996).
55. Blöchl, P. E. Projector augmented-wave method. *Phys. Rev. B* **50**, 17953–17979 (1994).
56. Perdew, J. P., Burke, K. & Ernzerhof, M. Generalized gradient approximation made simple. *Phys. Rev. Lett.* **77**, 3865–3868 (1996).
57. Perdew, J. P. et al. Restoring the density-gradient expansion for exchange in solids and surfaces. *Phys. Rev. Lett.* **100**, 136406 (2008).
58. Kawamura, M. FermiSurfer: Fermi-surface viewer providing multiple representation schemes. *Comput. Phys. Commun.* **239**, 197–203 (2019).
59. Marzari, N. & Vanderbilt, D. Maximally localized generalized Wannier functions for composite energy bands. *Phys. Rev. B* **56**, 12847–12865 (1997).
60. Kautzsch, L. et al. Structural evolution of the kagome superconductors AV_3Sb_5 (A=K, Rb, and Cs) through charge density wave order. *Phys. Rev. Mater.* **7**, 024806 (2023).
61. Ortiz, B. R. et al. CsV_3Sb_5: a $\mathbb{Z}_2$ topological kagome metal with a superconducting ground state. *Phys. Rev. Lett.* **125**, 247002 (2020).
62. Xiang, Y. et al. Twofold symmetry of c-axis resistivity in topological kagome superconductor CsV_3Sb_5 with in-plane rotating magnetic field. *Nat. Commun.* **12**, 6727 (2021).

Acknowledgements We thank Y. T. Song for the assistance with the low-temperature single-crystal X-ray diffraction measurements. This work is supported by the National Natural Science Foundation of China (grant nos. 12050003, 12004337, 12025408, 11921004, 12374142, 12304170, 12204298, 12274364 and 12274369), the National Key R&D Program of China (grant nos. 2022YFA1403202, 2023YFA1406100 and 2022YFA1403402), the Key R&D Program of Zhejiang Province, China (grant no. 2021C01002), the Strategic Priority Research Program of the Chinese Academy of Sciences (CAS) (grant nos. XDB33000000 and XDB33010100) and the Outstanding Member of Youth Promotion Association of CAS (grant no. Y2022004). The high-pressure experiments and the NMR experiments were carried out at the Cubic Anvil Cell and the High-field NMR stations of Synergic Extreme Condition User Facility, respectively.

Author contributions G.-H.C. coordinated the work, co-conceived the experiments with Y.L. and interpreted the results in discussion with J.-G.C., R.Z., J.-K.B., Y.L., X.-F.X. and C.C. The high-pressure experiments were performed by Z.-Y.L., P.-T.Y. and B.-S.W. under the leadership of J.-G.C.; J.-K.B. contributed to the structural analysis with help from J.-Y.Liu. The NMR measurement was done by Q.-X.S., J.L. and J.Y., supervised by R.Z. The theoretical calculations were made by L.-W.J., S.-Q.W., C.-C.X., H.J. and C.C. The crystals were grown by Y.L., W.-L.C., J.-Y.Lu. and C.-C.L. The ambient-pressure physical property measurements were done by Y.L., W.-Z.Y., Q.T., Z.R. and Z.-A.X. The paper was written by G.-H.C., J.-G.C., R.Z., J.-K.B., Y.L. and Z.-Y.L. All authors commented on the paper.

Competing interests The authors declare no competing interests.

Additional information

Supplementary information The online version contains supplementary material available at https://doi.org/10.1038/s41586-024-07761-x.

Correspondence and requests for materials should be addressed to Rui Zhou, Jin-Guang Cheng or Guang-Han Cao.

Peer review information *Nature* thanks Brenden Ortiz and the other, anonymous, reviewer(s) for their contribution to the peer review of this work. Peer reviewer reports are available.